


Article

Antibacterial Properties of Three-Dimensional Flower Cluster ZIF-L Modified by N-Doped Carbon Dots

Jing He, Yuanyuan Xiong, Huaixuan Mu, Peini Li, Yiqing Deng, Wangcai Zou and Qiang Zhao * 

School of Chemical Engineering, Sichuan University, No. 24 South Section 1, Yihuan Road, Chengdu 610065, China

* Correspondence: zhaoqiang@scu.edu.cn; Tel.: +86-15184325181

Abstract: To overcome the problems of excessive ion release of inorganic antimicrobial agents and the biological toxicity of organic antimicrobial agents, metal organic framework (MOF) materials are attracting attention in the antimicrobial field due to their tunable structural properties and multifunctional applications. Most current studies are limited to zeolitic imidazolate framework-8 (ZIF-8), which has low antimicrobial efficiency by component release. Two-dimensional (2D) zeolitic imidazolate framework nanoleaf (ZIF-L) possesses better antimicrobial effect than ZIF-8 because of the physical destruction to bacteria by its blade tip. However, the in-situ synthesis method of two-dimensional ZIF-L, and the problem of leaf accumulation, limit the wider application of ZIF-L. In this paper, three-dimensional (3D) flower cluster-like ZIF-L (2–3 μm , +31.23 mV), with better antibacterial effects and a wider application range, was prepared by stirring without adding other reagents. To further improve the antibacterial performance of ZIF-L, nitrogen-doped carbon dots (NCDs) were electrostatically absorbed by ZIF-L to obtain NCDs@ZIF-L composites. The NCDs@ZIF-L composites showed over 95% and 85% antibacterial efficiency against *E. coli* and *S. aureus*, respectively, at a concentration of 0.25 mg/mL. In addition, polylactic acid (PLA) films mixed with ZIF-L and NCDs@ZIF-L composites with PLA showed good antimicrobial properties, indicating the applicability of ZIF-L and NCDs@ZIF-L composites for antibacterial materials. With a unique three-dimensional crystal shape and positive surface charge, ZIF-L and NCDs@ZIF-L composites exhibited excellent antibacterial properties, which provided a new perspective for the study of antimicrobial materials.



Citation: He, J.; Xiong, Y.; Mu, H.; Li, P.; Deng, Y.; Zou, W.; Zhao, Q.

Antibacterial Properties of Three-Dimensional Flower Cluster ZIF-L Modified by N-Doped Carbon Dots. *Crystals* **2023**, *13*, 564. <https://doi.org/10.3390/cryst13040564>

Academic Editor: Volodymyr Bon

Received: 3 March 2023

Revised: 22 March 2023

Accepted: 23 March 2023

Published: 25 March 2023



Copyright: © 2023 by the authors. Licensee MDPI, Basel, Switzerland. This article is an open access article distributed under the terms and conditions of the Creative Commons Attribution (CC BY) license (<https://creativecommons.org/licenses/by/4.0/>).

Keywords: metal organic framework; zeolitic imidazole frameworks; composite materials; antibacterial

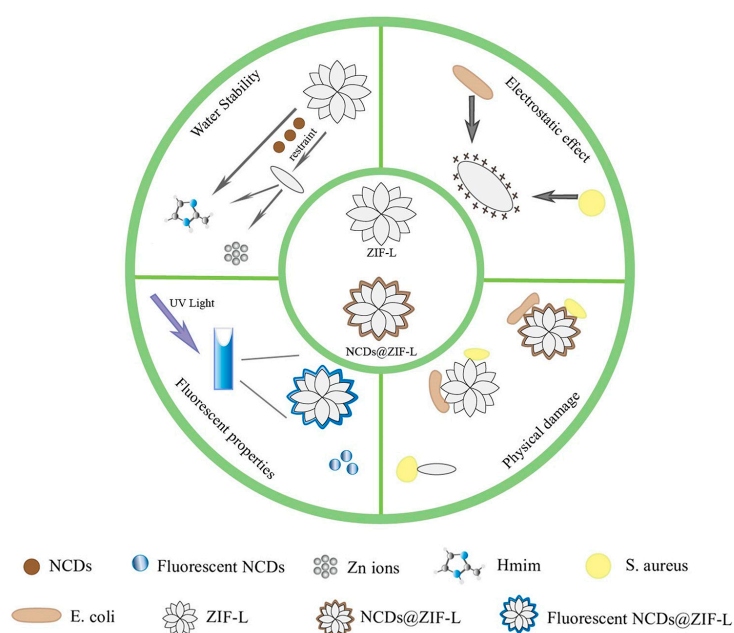
1. Introduction

Over the past few years, microbial infections have attracted more widespread attention than ever before from researchers and the public [1–3]. According to a recent research report, the number of deaths related to bacterial infection reached 7.7 million in 2019, making it the second leading cause of death in the world [4]. Moreover, antibiotic abuse has led to the emergence of multi-drug resistant pathogens (MDR), which has exacerbated the problem of bacterial infections [5,6]. In response to the abuse of antibiotics and the emergence of MDR, the development of highly efficient antimicrobial materials has attracted the attention of researchers in the field of nanotechnology and materials science [7,8].

Many antimicrobial materials, including metal ions [9,10], photocatalytic semiconductors [11,12], organic small molecules [13,14], and carbon-based nanomaterials [15–17], have been extensively studied. Among them, metal-organic frameworks (MOFs) [18–20], materials represented by zeolitic imidazolate frameworks (ZIFs), have become new research hotspots because they have shown advantages in overcoming the excessive metal ion release [9] and low light absorption efficiency of photocatalytic materials [21]. ZIF-L, formed by linking zinc ions and the organic ligand 2-methylimidazole (Hmim), has the same structural unit as ZIF-8 [22]. Both ZIF-L and ZIF-8 have good antibacterial properties, releasing Zn ions and imidazole-like antibacterial organic ligands [23]. Furthermore, ZIF-L has a unique structure

that can physically damage bacterial cells, and has a better killing effect on various bacteria, including MDR [24,25]. Moreover, it is more economical and environmentally friendly due to its aqueous solvent synthesis method and lower metal–organic ligand ratio [26]. ZIF-L is usually expressed as a two-dimensional (2D) blade shape, and has been mainly used in the form of a 2D nano-dagger in the antibacterial field. A ZIF-L nano-dagger is typically grown in situ on the surface of the target materials, and prevents bacterial growth by destroying adherent microbial cells through its sharp tips [27–29]. Although 2D ZIF-L has shown excellent antimicrobial properties, there are still some issues. For example, in situ synthesis methods are cumbersome and destructive to most materials, and the accumulation of 2D ZIF-L reduces its antimicrobial efficiency, which limits its application [30,31].

In this study, a stable three-dimensional (3D) flower cluster-like morphology of ZIF-L, with 2D ZIF-L sharp tips, was prepared. The 3D ZIF-L was synthesized with simple stirring, without adding other auxiliary reagents, and overcame the problems of damage to the target materials during in situ growth of 2D ZIF-L, which made 3D ZIF-L more widely applicable. At the same time, nitrogen-doped carbon dots (NCDs) were compounded onto ZIF-L by simple stirring. Maintaining the cluster morphology of 3D ZIF-L, NCDs@ZIF-L composites also showed better stability and antimicrobial effect, which provides ZIF-L materials a wider application prospect in the field of antibacterial materials. Polylactic acid (PLA), with good biocompatibility and complete degradability, is widely used in biomedical applications, and is necessary to provide PLA antimicrobial properties. Here, ZIF-L and NCDs@ZIF-L composites were compounded with PLA to obtain composite films. The prepared PLA composite membranes exhibited good antibacterial properties in antibacterial experiments, which confirmed the applicability of ZIF-L and NCDs@ZIF-L composites. (Scheme 1)



Scheme 1. Schematic diagram of the main properties of 3D ZIF-L and NCDs@ZIF-L composites.

2. Materials and Methods

2.1. Materials

2-Methylimidazole (Hmim, 98%) was purchased from Chengdu Zhuopu Instrument Co., Ltd. (Chengdu, China) Zinc nitrate hexahydrate ($\text{Zn}(\text{NO}_3)_2 \cdot 6\text{H}_2\text{O}$, 99%), citric acid (CA, 99%), and diethylenetriamine (DETA, 99%) were purchased from Chengdu Cologne Chemical Co., Ltd. (Chengdu, China) Polylactic acid (PLA) was purchased from Chengdu Nanding Medical Material Co.(Chengdu, China) All reagents were analytical grade and used without further purification. The *Escherichia coli* (*E. coli*) ATCC 25923 and *Staphylococcus aureus*

(*S. aureus*) ATCC 29213 used in the antimicrobial experiment were purchased from the Beijing Microbiological Cultural Collection Center (BJMCC). Mouse epithelial fibroblast L929 cells were obtained from the National Engineering Research Center for Biomaterials (Sichuan University). All water used in this study was deionized water (18.2 M Ω) prepared by the ultrapure water system (RES.J Scientific Instruments Co., Ltd, Xiamen, China).

2.2. Synthesis of ZIF-L and NCDs@ZIF-L Composites

Synthesis of ZIF-L: A total of 0.003 mol of zinc nitrate hexahydrate and 0.024 mol of Hmim were separately dissolved in 60 mL of deionized water. After dissolution, zinc nitrate solution was slowly added to the Hmim solution, magnetic stirred for 24 h at room temperature, then allowed to stand for 24 h. The solution was centrifuged at 8000 r/min for 10 min, washed three times to remove excess Hmim, and vacuum dried at 60 °C to collect.

Synthesis of NCDs: NCDs were synthesized by the one-step hydrothermal method. A total of 0.008 mol of citric acid was dissolved in 20 mL of deionized water. Then, 1 mL diethylenetriamine (DETA) was added and the solution was magnetic stirred to mix well. Then, the solution was put into a polytetrafluoroethylene autoclave and heated to 200 °C for 5 h. Once cooled to room temperature, the solution was removed from the reactor and filtered with a 0.22 μ m filter membrane. The filtered liquid was dialyzed in a 500 Da dialysis bag with deionized water for 24 h, and the inner solution was freeze-dried to obtain powder.

Synthesis of NCDs@ZIF-L composites: The composite materials were synthesized by adjusting the reaction time and raw material ratio. A mass ratio of 4:1 of ZIF-L and NCDs was added to 20 mL of deionized water. The solution was magnetic stirred for 4 h at room temperature, centrifuged at 8000 r/min to obtain the precipitate, and vacuum dried at 60 °C to collect powder.

2.3. Characterizations

The morphologies of ZIF-L and NCDs@ZIF-L composites were characterized by transmission electron microscopy (TEM, Talos F200S G2, Waltham, MA, USA). The powder X-ray diffraction (XRD) patterns were detected using a Rigaku Ultima IV diffractometer with Cu K α radiation. Chemical compositions of materials were studied using Fourier infrared spectroscopy (IR, NEXUS 670, Madison, WI, USA) and X-ray photoelectron spectroscopy (XPS, Thermo Scientific K-Alpha, Waltham, MA, USA). The bonding energies were corrected using the standard peak position (284.8 eV) of carbon element. The UV-Vis spectra of the materials were measured by UV-Vis spectrophotometry (UV6100, Shanghai, China). The fluorescence spectra of materials were detected using a fluorescence spectrophotometer (F97-Pro, Shanghai, China). The surface morphologies of bacteria after material treatment were characterized by scanning electron microscopy (SEM, JSM 7610F, Akishima City, Japan). The Zeta potentials on the surface of the materials were measured using a nanoparticle size and Zeta potential analyzer (Malvern Zetasizer Nano ZS90, Malvern, UK). The results of the Propidium iodide (PI) staining and 33342 staining experiments were observed by fluorescence upright microscopes (XD-RFL, Ningbo, China) and photos were taken with color research-grade CCD cameras (S1UC01C/M, JPLY Technology, Guangzhou, China).

2.4. Water Stability Tests

ZIF-L and NCDs@ZIF-L composite powders were placed in deionized water at room temperature to study their water stability. The water stability performance of ZIF-L and NCDs@ZIF-L composites were quantitatively evaluated by UV-Vis spectrophotometer [32]. The absorbance of the organic ligand Hmim at 203 nm at different concentrations was measured by UV-Vis spectrophotometer and the standard curve of Hmim was established. The degradation of the materials was obtained by measuring the absorbance of the filtrate at 203 nm against the standard curve.

This was performed as follows: An amount of 20 mg synthesized material was dissolved in 10 mL of deionized water and placed at room temperature for 5 days. The solution was placed away from light to eliminate the effect of photodegradation of ZIF-L.

Samples were taken at intervals and filtered using a 0.22 μm filter membrane. The filtrate was measured for the absorbance at 203 nm.

Diluted hydrochloric acid was added to the sample solution and adjusted for acidity. The solution was held until completely clarified and its pH was measured to be 3–4. Then, the solution was placed in the dark for 72 h to study its stability and component release after acid adjustment. Samples were taken at intervals and measured for the absorbance of Hmim at 203 nm.

2.5. Antibacterial Tests

Culture of bacteria: Using Gram-negative *E. coli* and Gram-positive *S. aureus* as model pathogens, the antibacterial activity of samples was tested. Disposable inoculation rings were used to dip the purchased beveled preservation culture and lined up on the inverted plate. After inoculation, the plates were placed in a sterile incubator at 37 °C. After 16 h of incubation, several single colonies were picked up into sterile liquid medium. The liquid medium was incubated in a constant temperature incubator at 37 °C for 14 h. Then, the bacterial solution was adjusted to $\text{OD}_{600} = 0.3$ using liquid medium/sterile PBS for use.

Absorbance method: The bacterial solutions were diluted with sterile PBS to obtain a bacterial solution with $\text{OD}_{600} = 0.1$. A total of 1 mL of bacterial solution was pipetted into several sterile centrifuge tubes, and three material solutions were added. Then, the concentrations of materials were adjusted to 0.5 mg/mL. Sterile PBS was set up instead of material as a negative control group. After light/dark treatment for 2 h, the samples were incubated with the bacterial mixture in a constant temperature shaker chamber at 37 °C for 72 h, and 100 μL of the mixture was taken from each sample every 12 h and place in a 96-well plate. The absorbance of OD_{578} was measured by microplate reader (D2004W, Meiying Instrument Manufacturing Co., Ltd, Shanghai, China) to quantify the antimicrobial properties of the material.

Plate counting: The $\text{OD}_{600} = 0.3$ bacterial solution was diluted 10^6 times; the 100 μL bacterial solution was taken into several sterile centrifuge tubes, and then different concentrations of sample solutions were added to obtain a series gradient concentration of materials and bacterial mixtures. The mixtures were incubated in a constant temperature shaker chamber at 37 °C for 4 h. After incubation, 100 μL mixed solution was taken and evenly applied to the plates. Three plates were coated in each sample group, and sterile PBS was set up as a negative control group. The coated plates were incubated overnight in a 37 °C incubator, and colonies on the plates were counted the next day to quantify the antimicrobial properties of the materials.

2.6. Antibacterial Mechanism

The level of bacterial endogenous reactive oxygen species (ROS) was measured using an ROS kit of H2DCFH-DA loaded with a fluorescent probe. Non-fluorescent DCFH undergoes a redox reaction with the endogenous ROS produced in bacteria to produce fluorescent DCF. By detecting the fluorescence intensity of DCF, the amount of ROS generated in the bacteria can be obtained; this was used to measure the ROS generation of materials during the action of materials on bacteria.

Hoechst 33342 is a blue fluorescent dye that can penetrate cell membranes and is commonly used for apoptosis detection. After co-incubating the obtained material with the bacterial solution for a period of time, Hoechst 33342 working solution was added, stained thoroughly, washed, and observed under fluorescence microscope. The concentration of materials used in the staining experiment was 0.5 mg/mL, and PBS was set as the negative control group.

Propidium iodide (PI) dye was used to detect apoptosis after material treatment. PI is an embedded dye that can only pass through bacteria whose cell membranes are broken. PI stains DNA by passing through the broken bacterial cell membrane, binding to the DNA double strands, and emitting red fluorescence. The concentration of materials used in the staining experiment was 0.5 mg/mL, and PBS was set as the negative control group.

The adsorption effect of the material on bacteria was explored by measuring the surface Zeta potential of materials. Materials with different surface charges produced different degrees of electrostatic adsorption effects on bacteria. The effects of surface charge on the antimicrobial properties of the materials were investigated by comparing the Zeta charge of the materials.

By observing the SEM morphology of bacteria after treatment with PBS and materials, it can be seen that the morphological changes of the bacterial surface visually reflect the damage of the material to the bacterial cell.

2.7. Cytotoxicity Tests

Cytotoxicity is an important aspect of the transformation of metallic materials in biomedical and daily applications. Taking mouse epithelial fibroblast L929 cells as a model, the cytotoxicity of ZIF-L and NCDs@ZIF-L composites was explored by using a CCK8 kit.

A total of 30 mg of materials was dissolved in 6 mL of DMEM medium containing 12% fetal bovine serum solution (FBS) to obtain a stock solution of 5 mg/mL, placed at 37 °C with 5% CO₂, and incubated for 24 h. The supernatant was centrifuged and filtered using a 0.22 µm filter membrane to obtain 5 mg/mL of sample extract. The leachate was diluted to 2.5%, 5%, 10%, 20%, and 100%, and 100 µL was added to each 96-well plate. DMEM medium containing L929 cells without the extract was added as a control group. A total of 100 µL of L929 cell suspension was added to a 96-well plate and pre-cultured for 24 h (37 °C, 5% CO₂). The medium was removed, and 100 µL of infusion solution or control of the treatment medium was added to each well. Five parallel samples of each concentration were set up and incubated again for 24 h. The medium was removed and 10% of CCK8 solution was added to each well, incubated for 2 h at 37 °C. The OD₄₅₀ value of each well was assayed using a microplate reader.

2.8. Antibacterial Polylactic Acid (PLA) Films

In order to investigate applications in the antimicrobial field, the materials were laminated onto PLA films to test their applied antimicrobial properties. The PLA films were prepared by the cast film formation method [33], as follows: The material powder (1 g) and PLA (2 g) powder were dissolved in 40 mL of ethyl acetate. The mixture was ground by ball mill at 200 r/min for 1 h. After being well ground, it was poured into the mold, cooled overnight, dried at 60 °C, and collected. The PLA group without materials was also added as a negative control group. The PLA films were immersed in OD₆₀₀ = 0.3 bacterial solution and incubated in a constant temperature shaker chamber at 37 °C, and the absorbance was measured to quantitative analyze the change in bacterial concentration.

3. Results

3.1. Material Characterization

Figure 1a,b shows the TEM images of the ZIF-L and NCDs@ZIF-L composites. As can be seen, ZIF-L exhibited a 3D flower-like shape with uniform particle size of 2–3 µm, and NCDs@ZIF-L composites exhibited the same nanocrystal morphology. At the same time, compared with ZIF-L, the blade edges of NCDs@ZIF-L composites were rougher and more blurred. As shown in Figure 1c,d, the surface roughness of NCDs@ZIF-L composites increased compared to ZIF-L. According to the HRTEM image, lattice fringes of NCDs were shown on the flocs of the NCDs@ZIF-L composites. The lattice spacing of NCDs (Figure S1, Supplementary Materials) was 0.24 nm, which corresponded to the (100) crystal plane of graphitic carbon [34,35]. It was presumed that the NCDs were adsorbed onto the composite leaves' surfaces after the trace of Hmim was released by hydrolysis.

The surface charge was measured using a Zetasizer particle size analyzer. As shown in Figure 2a, NCDs had a negative Zeta potential (−5.65 mV), and ZIF-L had a high positive Zeta charge (+31.23 mV), while the Zeta potential of NCDs@ZIF-L composites was +10.83 mV. The decrease in the Zeta potential of NCDs@ZIF-L composites related

to the ZIF-L surface indicated that NCDs were adsorbed onto the ZIF-L surface through electrostatic interaction.

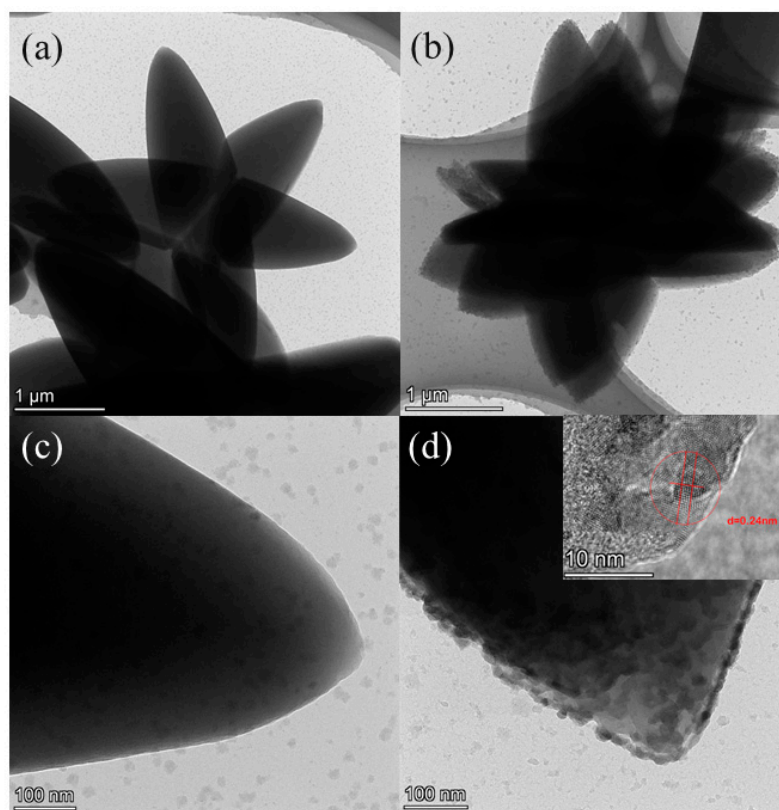


Figure 1. TEM images of ZIF-L (a,c) and the NCDs@ZIF-L composites (b,d) at a scale of 1 μm and 100 nm. The inset image shows HR-TEM result.

Figure 2b shows the XRD patterns of ZIF-L and the NCDs@ZIF-L composites. Compared with standard ZIF-L crystals [22,36], ZIF-L was successfully synthesized. The NCDs@ZIF-L composites, in the presence of NCDs, maintained the crystal morphology of ZIF-L. The absence of characteristic peaks of NCDs in the XRD of NCDs@ZIF-L composites might be caused by the uniform dispersion and low content of NCDs in the composites; this same phenomenon has been observed in other studies [37,38].

To explore the structures and elemental compositions of ZIF-L and NCDs@ZIF-L composites, we carried out XPS on the samples. As Figures 2c–f and S3 (Supplementary Materials) show, the XPS survey spectrum of ZIF-L and NCDs@ZIF-L composites demonstrated the presence of elements Zn, N, and C. As shown in the Zn 2p spectrum, the binding energy values of 1044.8 and 1021.7 eV correspond to the $2p_{3/2}$ and $2p_{1/2}$ components, respectively [37]. The C 1s spectra is divided into three peaks, at 284.68, 285.78, and 287.28 eV, which are assigned to the C=C bond, C-N bond, and C=O bond, respectively [39,40]. The N 1s spectra is divided into two peaks, and the peak at 398.78 eV is attributed to the organic ligand Hmim. The peak at 400.28 eV corresponds to the N–Zn bond, which is the characteristic peak of ZIF-L [41]. The XPS results of the NCDs@ZIF-L composites showed a trace presence of C=O bonds and a decrease in the content of N–Zn compared to ZIF-L. The presence of C=O bonds might be caused by the presence of NCDs, and the decrease in C–Zn might be caused by the trace hydrolysis of ZIF-L during the synthesis process.

The IR spectroscopy results (Figure S4, Supplementary Materials) of the materials showed that NCDs@ZIF-L composites displayed the same results as ZIF-L [42]. No characteristic peak of the C=O bond at 1700 cm^{-1} was found, and no new functional group appeared in FT-IR, probably because NCDs were complexed with ZIF-L by electrostatic adsorption.

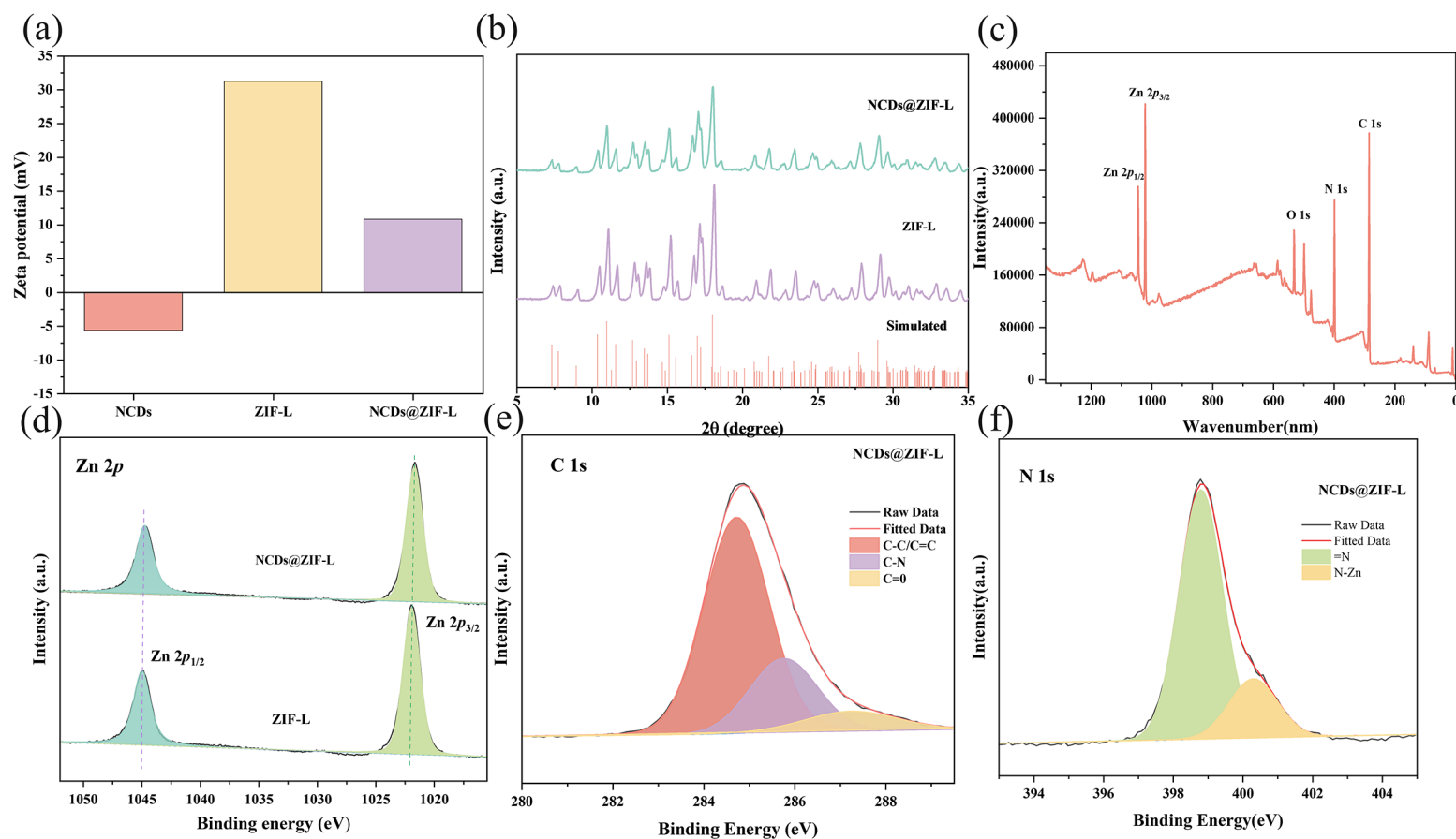


Figure 2. (a) Zeta potential comparison of NCDs, ZIF-L, and NCDs@ZIF-L composites. (b) XRD patterns of as-synthesized NCDs@ZIF-L and ZIF-L. XPS spectra of NCDs@ZIF-L composites: (c) full survey spectrum, (d) Zn 2p spectra, (e) C 1s spectra, and (f) N 1s spectra.

The sample solution showed only a peak at 203 nm related to ZIF-L in the UV-Vis spectra of NCDs@ZIF-L composites (Figure 3a). The peak at 203 nm is the same as the UV-Vis spectra of the Hmim solution (Figure S5a, Supplementary Materials). The absorption peaks of NCDs could not be found in the UV-Vis spectra of NCDs@ZIF-L composites; only absorption of Hmim was seen. Therefore, the component release of ZIF-L and NCDs@ZIF-L composites in solution can be explored by comparison to standard curve of Hmim (Figure S5b, Supplementary Materials).

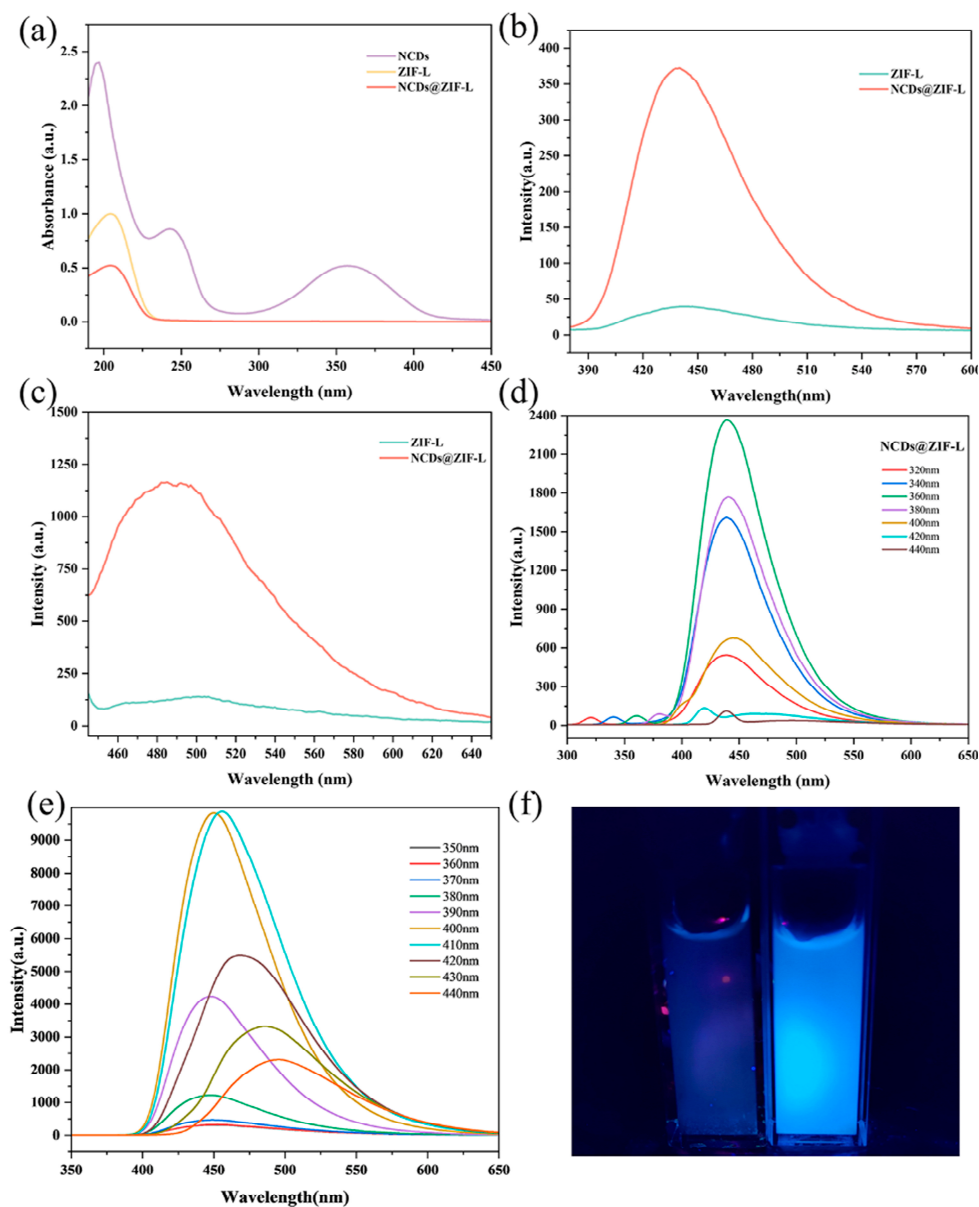


Figure 3. (a) UV-Vis absorption of NCDs, ZIF-L, and NCDs@ZIF-L composites. Fluorescence spectra of NCDs, ZIF-L, and NCDs@ZIF-L composites: (b) excited at 360 nm and (c) excited at 430 nm. Fluorescence spectra of (d) NCDs@ZIF-L composites and (e) NCDs under various excitation wavelengths. (f) ZIF-L and NCDs@ZIF-L composites solutions irradiated by UV lamp.

Fluorescence is a typical property of NCDs [43], and the fluorescence performance of ZIF-L and NCDs@ZIF-L was studied. As shown in Figure 3b, when the excitation wavelength was 360 nm, NCDs@ZIF-L composites showed a blue fluorescence at 440 nm that was not found in ZIF-L. When the excitation wavelength was changed to 430 nm, fluorescence at 490 nm was seen in NCDs@ZIF-L composites. Comparing the fluorescence

figure of ZIF-L and NCDs, it was confirmed that the fluorescence properties in the complexes originated from NCDs. At the same time, NCDs@ZIF-L composites exhibited the wavelength-dependent excitation behavior of NCDs [44–46]. These all prove the presence of NCDs in the NCDs@ZIF-L composites.

From the above characterization results, it is clear that NCDs were adsorbed onto the ZIF-L petal surface due to electrostatic interactions. The NCDs uniformly dispersed on the ZIF-L petal surface and wrapped the surface of the ZIF-L blades, slowing down the hydrolysis of ZIF-L. At the same time, the NCDs did not damage the ZIF-L crystal structure, thus preserving the physical sterilization effect of the sharp tips of ZIF-L. Meanwhile, the addition of NCDs creates NCDs@ZIF-L composite fluorescent properties, which broadens the application possibilities of ZIF-L.

3.2. Water Stability

For the wide water-related application of ZIF-L materials, it is crucial to study their water stability. Hence, the UV-Vis spectrum of the organic ligand Hmim in ZIF-L (Figure S5, Supplementary Materials) was established to quantitatively study the stability of ZIF-L and NCDs@ZIF-L composites in an aqueous environment.

As Figure 4a–c shows, comparing the steady-state release curves of ZIF-L and NCDs@ZIF-L composites, it could be seen that NCDs@ZIF-L composites showed a lower degradation rate from the initial stage. Therefore, NCDs@ZIF-L composites were more stable in an aqueous environment. Previous studies have shown that the hydrolysis of ZIF structures can be seen as the reverse of synthesis the process [47]. It was speculated that the Hmim released by ZIF-L encapsulates ZIF-L blades and slows down the hydrolysis of ZIF-L [32]. Here, NCDs@ZIF-L composites had a lower degradation efficiency, which might be due to NCDs wrapped around ZIF-L blades, effectively insulating contact with H₂O.

In order to study the release of ZIF-L and NCDs@ZIF-L composites in an acidic environment, diluted hydrochloric acid was added to adjust the sample solution to acidic. After the addition of acid, the white turbid liquid gradually changed into colorless transparent solutions, thus defining the complete disintegration of ZIF-L and NCDs@ZIF-L composites. The pH of the solution was measured to be 3–4. At the same time, the solution after acid hydrolysis was irradiated with an ultraviolet lamp, and blue fluorescence excited by NCDs was displayed in the NCDs@ZIF-L composites solution. The degradation of ZIF-L and NCDs@ZIF-L composites in an acidic environment was explored by measuring the release of Hmim at different times (Figure 4d). During the first hour, ZIFs degraded rapidly. At the 72nd hour, the absorbance of Hmim was at a stable level, at which time the degradation rates of ZIF-L and NCDs@ZIF-L composites were considered as 100%. The results demonstrated that both ZIF-L and NCDs@ZIF-L composites had a rapid and good response to acidic stimuli. To further investigate the water stability of ZIF-L and NCDs@ZIF-L composites, XRD and FT-IR tests were performed on the materials after 15 days immersion, and the results are shown in Figure 4e, f. After a long period of immersion, the XRD patterns of ZIF-L showed changes, while the changes in the NCDs@ZIF-L composites were subtle. According to the IR results, the internal structures of ZIF-L and NCDs@ZIF-L composites did not change. The above results demonstrated that ZIF-L maintained good stability in an aqueous environment for a short period of time, while some changes, which did not change the internal structure, occurred with time extension. In contrast, NCDs@ZIF-L composites showed more persistent stability in an aqueous environment. The crystal structure of the 3D clusters made ZIF-L have good water stability. Meanwhile, for NCDs@ZIF-L composites, the NCDs were wrapped around the leaf surface of ZIF-L and thus blocked the reaction between ZIF-L and H₂O, which made NCDs@ZIF-L composites have better water stability than ZIF-L. The properties of ZIF-L and NCDs@ZIF-L composites to remain stable in aqueous environments and respond quickly to acidic environments make ZIF-L materials more widely usable in aqueous environments.

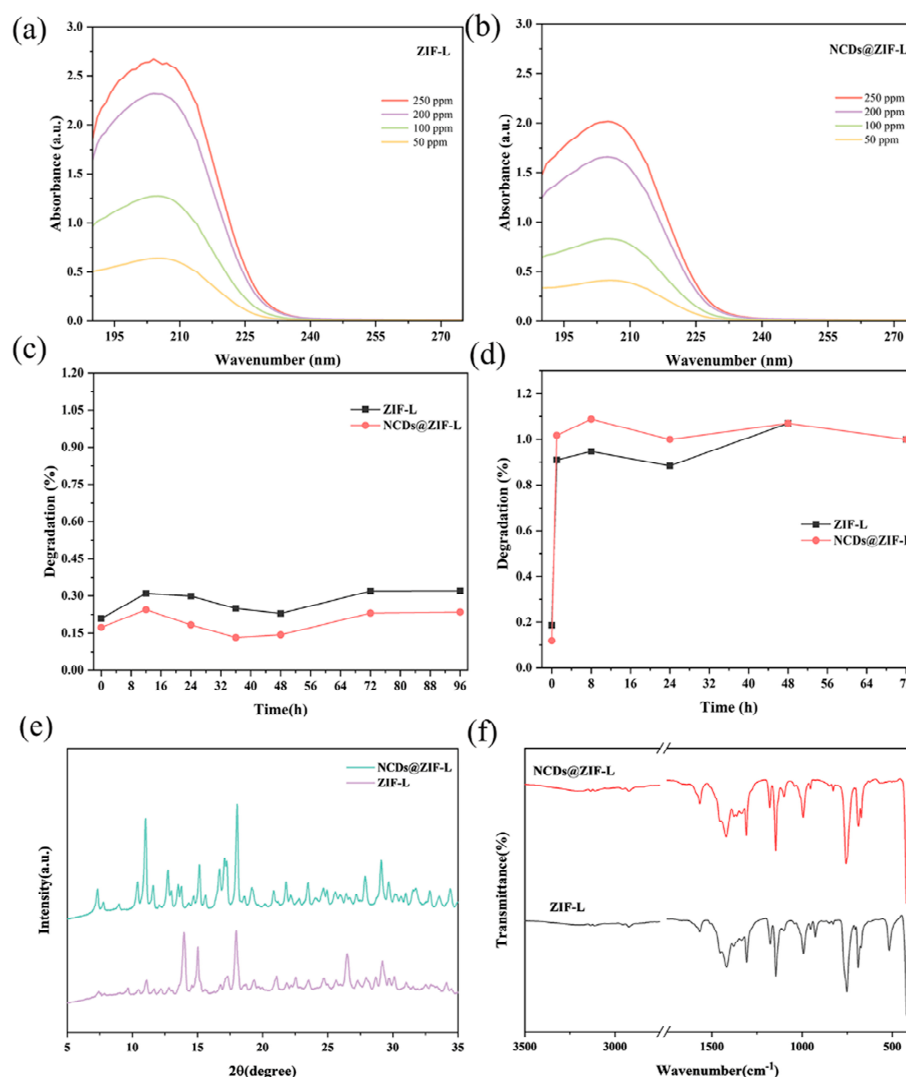


Figure 4. UV-Vis spectra of ZIF-L (a) and NCDs@ZIF-L composites (b) in DI water at different concentrations; degradation rate (%) of ZIF-L and NCDs@ZIF-L composites at different immersion times in DI water (c) and in acidic solutions (d); XRD (e) and FT-IR spectra (f) of ZIF-L and NCDs@ZIF-L composites after prolonged immersion.

3.3. Antibacterial Activity

The excellent antibacterial effects of ZIF-L and NCDs@ZIF-L composites were proved by plate counting and OD₆₀₀ measurement, and NCDs@ZIF-L composites showed better antibacterial properties than ZIF-L.

In order to confirm the inhibitory effect of the material on bacterial growth at different times, OD₆₀₀ measurement was used to test the growth of bacteria in a co-culture of *E. coli* or *S. aureus* and materials. Considering the influence of lighting in the application scenario, the antibacterial experiments added a light. The results of the antibacterial experiments against *E. coli* showed that the absorbance of both the ZIF-L group and the NCDs@ZIF-L composite group remained at a low level for 48 h (Figure 5a). At a material concentration of 0.5 mg/mL, the absorbance values of the ZIF-L group always remained below 0.16, and the absorbance values of the composite group always remained below 0.08, indicating that the growth of bacteria was well inhibited. Similar results were seen in the antibacterial experiments against *S. aureus* (Figure 5b). The absorbance values of the ZIF-L group remained below 0.15, and those of the composite group remained below 0.1 throughout the process. At low concentrations, both ZIF-L and NCDs@ZIF-L composites showed excellent antibacterial effects in the antibacterial experiments, and the composites exhibited better antibacterial effects.

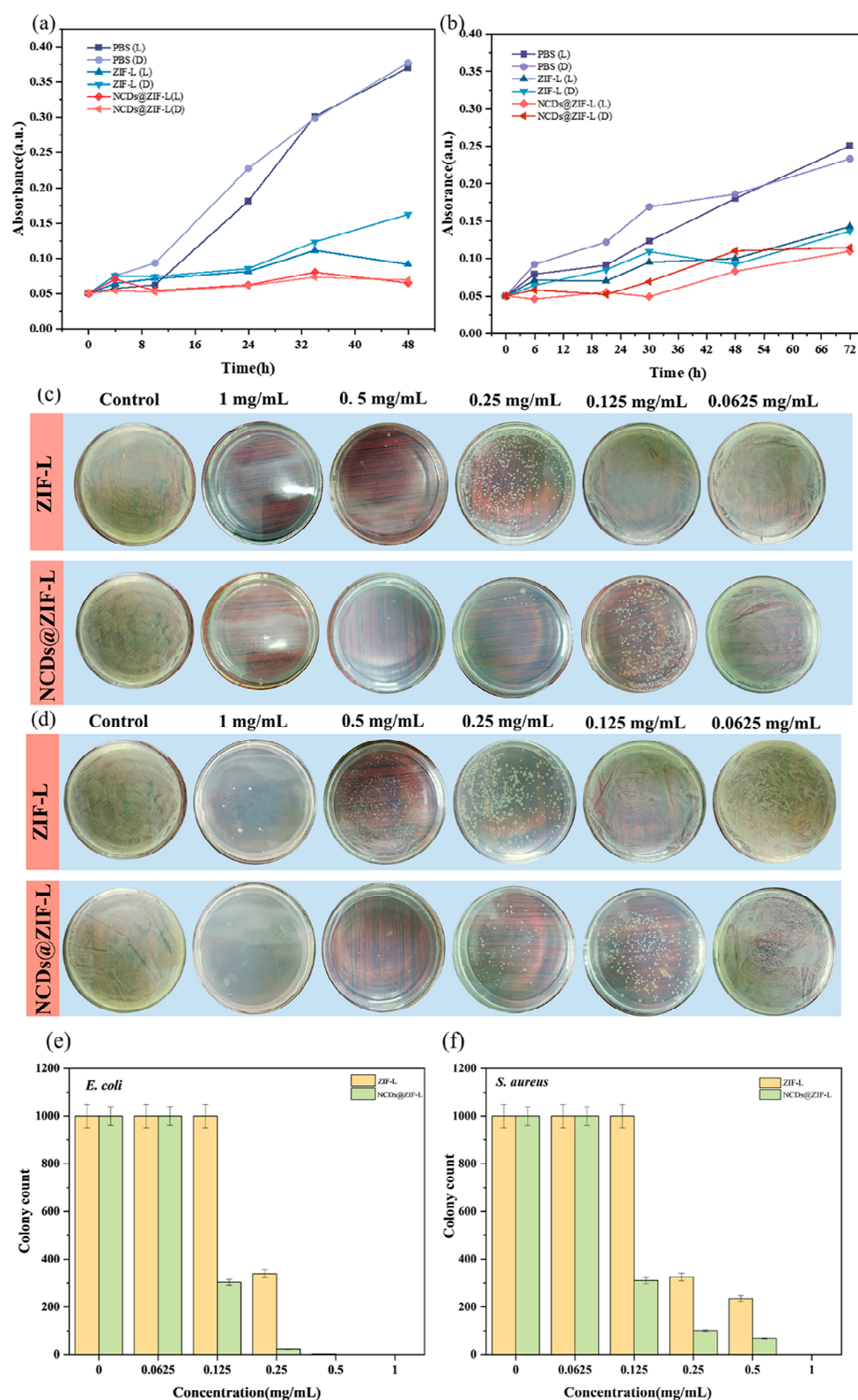


Figure 5. Antibacterial test results. The OD₆₀₀ method measures the antibacterial performance of the material against (a) *E. coli* and (b) *S. aureus* at different times. Bacterial survival of *E. coli* (c) and *S. aureus* (d) after treatment with materials of different concentrations. Colony count after material treatment: *E. coli* (e) and *S. aureus* (f).

Plate counting was used to evaluate the antimicrobial properties of different concentrations of materials against *E. coli* and *S. aureus*. The results of the antimicrobial activity of ZIF-L and NCDs@ZIF-L composites are shown in Figures 5c–f and S6. The results showed that ZIF-L had good antibacterial effect when the concentration was higher than 0.25 mg/mL, while NCDs@ZIF-L composites showed considerable antibacterial effect at a concentration of 0.125 mg/mL. At a concentration of 0.25 mg/mL, the NCDs@ZIF-L composites exhibited much better antibacterial activity than ZIF-L, killing 99% of *E. coli* and *S. aureus*. Compared with pure ZIF-L, the introduction of NCDs improved the antibacterial properties of the material.

The minimum inhibition concentration (MIC) of ZIF-8 against *E. coli* and *S. aureus* by releasing metal ions and organic ligands is usually above 10 mg/mL [48]; the MIC of 2D ZIF-L powder with sharp tips was 2.5 mg/mL against *E. coli* [49]. In comparison, ZIF-L and NCDs@ZIF-L composites with 3D flower clusters showed better antibacterial effect. The good antimicrobial properties of ZIF-L and NCDs@ZIF-L composites at lower concentrations provide a good performance basis for their applications in biosterilization environments, as well as daily sterile environments.

3.4. Antibacterial Mechanism

According to the results of the Zetasizer particle size analyzer, both ZIF-L and NCDs@ZIF-L composites had positive potentials. Zeta potential tests were performed on the *E. coli* and *S. aureus* used in the experiment, both of which carried high negative potentials (Figure 6a). The ZIF-L and NCDs@ZIF-L composites with positive potential had an electrostatic adsorption effect on bacteria with high negative potential, causing the bacteria to adsorb onto the surface of the material and changing the bacterial surface potential. Based on the antibacterial results and potential changes, it is clear that ZIF-L and NCDs@ZIF-L are more effective against *S. aureus* than *E. coli*. This is because Gram-positive bacteria, represented by *S. aureus*, possess a thicker peptidoglycan cell wall structure, while Gram-negative bacteria, represented by *E. coli*, have a thinner cell wall. The electrostatic adsorption of the materials to bacteria was the first step in the antimicrobial process and laid the foundation for further action of the materials on bacteria.

In addition, to investigate the effect of ROS during the antimicrobial process of the materials, an H2DCFH kit was used to detect the amount of ROS production during the co-culture of the materials with bacteria. According to the results (Figure 6b), the fluorescence intensity of DCF was maintained at a low level for 120 min, with or without increasing the light. The results proved the absence of ROS production during the antimicrobial process of the materials.

Hoechst 33342 dye was used to detect apoptosis of bacterial cells after material treatment. Apoptotic cells have dense and fragmented stains due to DNA breaks that bind better to Hoechst 33342 dye. After ZIF-L and NCDs@ZIF-L composite treatment, the *E. coli* and *S. aureus* groups showed local dense staining, indicating apoptosis of bacterial cells. The killing effects of ZIF-L and NCDs@ZIF-L composites on bacteria were verified.

In order to further verify the physical damage of ZIF-L and composites to bacterial cell walls and membranes, the PI reagent was used to detect bacterial apoptosis. As shown in Figures 6d and S7, after PI staining of the co-culture with the materials, *E. coli* and *S. aureus* showed obvious red fluorescence, which indicated the emergence of PI-DNA and serious damage to the surface of bacteria. Due to the electrostatic adsorption of the materials onto bacteria, the red fluorescence mainly appeared around the agglomerated material after PI staining. The PI staining results showed that the adsorption of the materials onto the bacteria caused damage to the bacterial cell membrane, which in turn led to further bacterial death.

The disruption of bacterial cell membranes by the materials and the effects on bacterial morphologies were further investigated by comparing the SEM images of bacteria after material treatment (Figure 7). Based on the SEM results of the bacteria, both *E. coli* and *S. aureus*, in the sterile PBS group, grew well, with smooth and flat surfaces, while the morphology of both *E. coli* and *S. aureus* after ZIF-L and NCDs@ZIF-L composite treatment

showed some aberrations. Among them, the morphological changes of the bacteria were more obvious in the NCDs@ZIF-L composite group. This was consistent with the results of the antimicrobial test, where NCDs@ZIF-L composites had an increased effect on the bacteria. As seen in Figure 7, the bacteria were adsorbed onto the surface of the materials and caused some degree of breakage. The destructive effects of ZIF-L and NCDs@ZIF-L composites on bacteria were demonstrated.

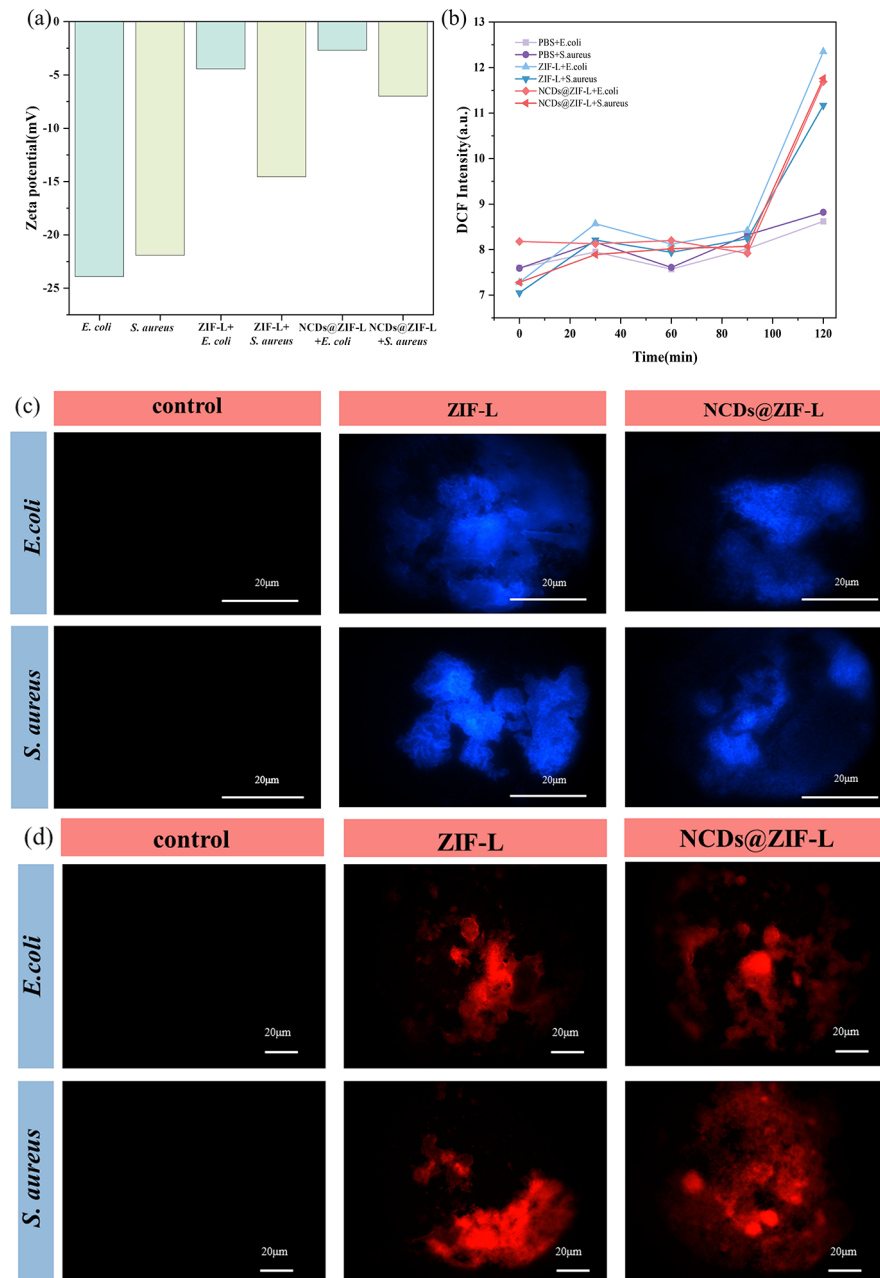


Figure 6. Antibacterial mechanism. (a) Zeta potential of *E. coli* and *S. aureus* after treated. (b) ROS production at different times of co-culture of bacteria and materials. Fluorescence images of bacteria stained with 33342 dye (c) and PI staining (d) after material treatment.

According to the characterization test results, the antibacterial process of materials was as follows: Bacteria with negative surface potential were adsorbed onto the surface of materials with positive surface charge. The cross-petal structure of ZIF-L played a fixed and dispersing role for bacteria, and the sharp tip destroyed adherent bacterial cells to prevent bacterial growth. According to the results of the water stability experiment, NCDs@ZIF-L

have better stability, which means that the encapsulation of NCDs makes ZIF-L more inclined to maintain a three-dimensional morphology, with better antimicrobial effect. The physical bactericidal effect of the material is related to its surface state. According to the TEM results, it can be seen that NCDs are uniformly distributed on the surface of ZIF-L, and the surface roughness of the composite is enhanced, thus exhibiting a superior antimicrobial effect relative to ZIF-L.

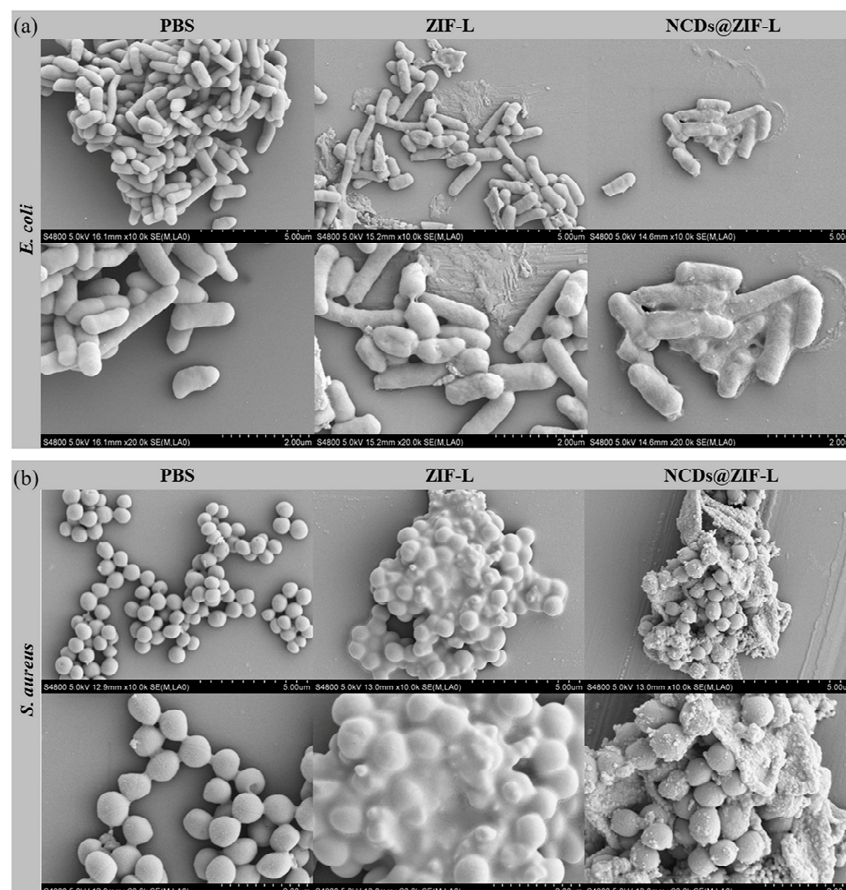


Figure 7. SEM images of *E. coli* (a) and *S. aureus* (b) after treatment with sterile PBS, ZIF-L, and NCDs@ZIF-L composites.

Based on structural composition, both ZIF-L and ZIF-8 can achieve an antimicrobial effect by releasing Zn ions and Hmim. However, ZIF-L has low solubility in aqueous environments, and the effect of ions and ligands, released in trace amounts, on the antimicrobial results was minimal in previous studies investigating the antimicrobial mechanism of ZIF-L [50,51]. Thus, the ions and ligands released from ZIF-L are considered here to have a small effect on the antimicrobial effect.

3.5. Cytotoxicity Test

The cytotoxicity of ZIF-L and NCDs@ZIF-L composites was explored using mouse epithelial fibroblasts L929 cells as a model. A group containing no material was set up as a control. As seen in Figure 8, when the concentrations of the extracts were 1, 0.5, 0.25, and 0.125 mg/mL, the ZIF-L and NCDs@ZIF-L groups showed high cell survival and low cytotoxicity. When the concentration of the materials was 5 mg/mL, the cell survival rates of the ZIF-L and NCDs@ZIF-L groups were above 90%, and the cell survival rate of the NCDs@ZIF-L group was higher than that of ZIF-L group, indicating the lower cytotoxicity of NCDs@ZIF-L. The cell test results demonstrated the good biosafety of ZIF-L and NCDs@ZIF-L. The low cytotoxicity of ZIF-L and NCDs@ZIF-L laid a good foundation for biological application, and made in vivo and in vitro applications possible.

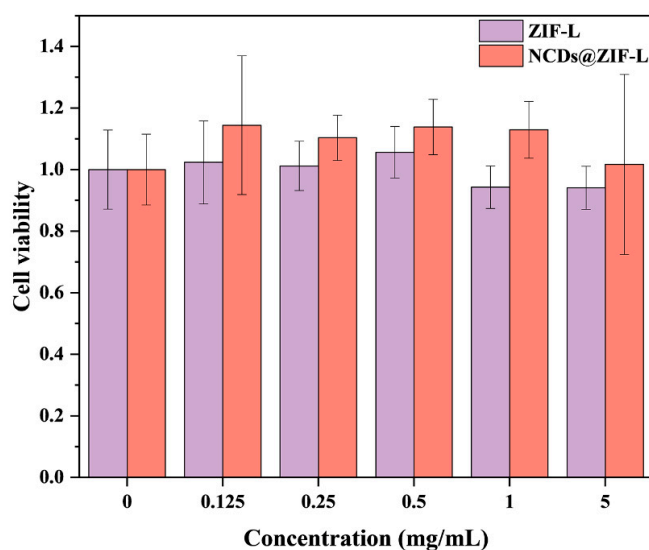


Figure 8. Toxicity results of ZIF-L and NCDs@ZIF-L on L929 cells obtained by CCK8 method experiments.

3.6. Antibacterial PLA Films

To explore the application of the materials in the antimicrobial field, the materials were dissolved with PLA in ethyl acetate to obtain PLA composite films. The antimicrobial performances of ZIF-L materials in the target materials were discussed by carrying out antimicrobial tests on the PLA films.

The composite films obtained by adding ZIF-L and NCDs@ZIF-L composites were prepared. After grinding, the added materials did not play too much of a role in changing the shape of PLA films. The PLA composite films were immersed in PBS and irradiated with a UV lamp to observe the fluorescence properties. As shown in Figure 9a,b, the PLA film with NCDs@ZIF-L composites, added after a period of immersion, showed blue fluorescence under the UV lamp. The introduction of NCDs@ZIF-L composites conferred new fluorescent properties to PLA films. According to Figure 9c, the PLA composite films prepared by adding materials, compared to the PLA films, remained at low values of OD₆₀₀ after 48 h. This proves that the ZIF-L@PLA and NCDs@ZIF-L@PLA composite films have a good inhibitory effect on the growth of *E. coli* and *S. aureus*. The fluorescent properties and good antibacterial properties to PLA composite films further expanded the biological applications of PLA films. This also demonstrates the potential of ZIF-L and NCDs@ZIF-L composites in biomedical applications.

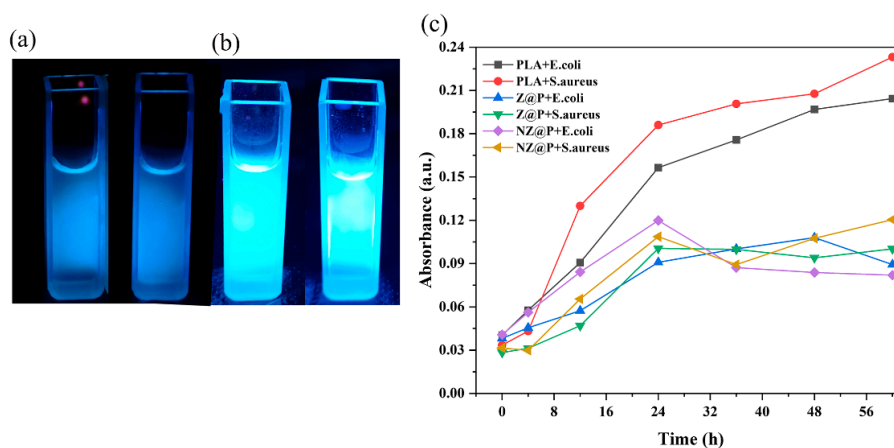


Figure 9. PLA composite films immersion solution image under UV light: (a) ZIF-L@PLA film, (b) NCDs@ZIF-L@PLA film, and (c) OD₆₀₀ values of PLA composite films co-cultured with *E. coli* and *S. aureus* for 48 h.

4. Conclusions

The three-dimensional flower cluster ZIF-L was prepared by carefully controlling the reaction conditions, and NCDs with negative surface potential were compounded onto the three-dimensional ZIF-L by electrostatic adsorption to obtain NCDs@ZIF-L composites. Experiments results indicated that ZIF-L and NCDs@ZIF-L composites had good stability in aqueous environments, for a short period of time, and a quick response to acidic stimuli. NCDs@ZIF-L composites exhibited longer stability in aqueous environments after 15 days immersion. ZIF-L and NCDs@ZIF-L composites both had good antibacterial properties and low cytotoxicity. The introduction of NCDs led to a decrease in the minimum antibacterial concentration of the composites to 0.125 mg/mL and a significant increase in the antibacterial effect; it also provided NCDs@ZIF-L composites with fluorescent properties. The NCDs adsorbed onto ZIF-L by electrostatic adsorption enhanced the antimicrobial properties by enhancing the surface roughness and stability of ZIF-L, although the charge on the material surface was reduced. PLA composite films were prepared by co-dissolving the materials with PLA by casting method, and the PLA composite films showed good antibacterial properties. The economical synthesis method and good performance of ZIF-L and NCDs@ZIF-L composites indicates that they have great potential and application value in the antibacterial field.

Supplementary Materials: The following supporting information can be downloaded at: <https://www.mdpi.com/article/10.3390/cryst13040564/s1>. Figure S1. TEM (a) and HR-TEM (b) image of NCDs.; Figure S2. Different morphologies of ZIF-L crystals in SEM tests.; Figure S3. XPS spectra of ZIF-L: (a) full survey spectrum, (b) C 1s spectra and (c) N 1s spectra.; Figure S4. FT-IR spectrum of NCDs@ZIF-L composites compared with ZIF-L (a) and NCDs (b).; Figure S5. (a) UV-Vis spectra of dissolved 2-methylimidazole in DI water at different concentrations; (b) a calibrated standard curve for determining the concentration of ligands in water.; Figure S6. Results of antibacterial rates of ZIF-L and NCDs@ZIF-L composites against *E. coli* (a) and *S. aureus* (b).; Figure S7. Images of bacteria stained with 33342 dye (a) and PI staining (b) under visible light after materials treatment.

Author Contributions: Conceptualization, Q.Z.; methodology, J.H.; validation, Y.X.; formal analysis, H.M.; investigation, P.L.; data curation, Y.D.; writing—original draft preparation, J.H.; visualization, W.Z.; funding acquisition, Q.Z. All authors have read and agreed to the published version of the manuscript.

Funding: This work was supported by Industry-university-research cooperation of Sichuan University (No.19H0340).

Data Availability Statement: The authors confirm that the data supporting the reported results can be found within the article. Other relevant information can be obtained from the authors.

Conflicts of Interest: The authors declare no conflict of interest.

References

1. Duan, S.; Wu, R.; Xiong, Y.-H.; Ren, H.-M.; Lei, C.; Zhao, Y.-Q.; Zhang, X.-Y.; Xu, F.-J. Multifunctional Antimicrobial Materials: From Rational Design to Biomedical Applications. *Prog. Mater. Sci.* **2022**, *125*, 100887. [CrossRef]
2. Hu, X.; Zhang, H.; Wang, Y.; Shiu, B.-C.; Lin, J.-H.; Zhang, S.; Lou, C.-W.; Li, T.-T. Synergistic Antibacterial Strategy Based on Photodynamic Therapy: Progress and Perspectives. *Chem. Eng. J.* **2022**, *450*, 138129. [CrossRef]
3. Li, B.; Luo, Y.; Zheng, Y.; Liu, X.; Tan, L.; Wu, S. Two-Dimensional Antibacterial Materials. *Prog. Mater. Sci.* **2022**, *130*, 100976. [CrossRef]
4. Ikuta, K.S.; Swetschinski, L.R.; Aguilar, G.R.; Sharara, F.; Mestrovic, T.; Gray, A.P.; Weaver, N.D.; Wool, E.E.; Han, C.; Hayoon, A.G.; et al. Global Mortality Associated with 33 Bacterial Pathogens in 2019: A Systematic Analysis for the Global Burden of Disease Study 2019. *Lancet* **2022**, *400*, 2221–2248. [CrossRef]
5. Privalsky, T.M.; Soohoo, A.M.; Wang, J.; Walsh, C.T.; Wright, G.D.; Gordon, E.M.; Gray, N.S.; Khosla, C. Prospects for Antibacterial Discovery and Development. *J. Am. Chem. Soc.* **2021**, *143*, 21127–21142. [CrossRef] [PubMed]
6. Ghosh, S.; Mukherjee, S.; Patra, D.; Haldar, J. Polymeric Biomaterials for Prevention and Therapeutic Intervention of Microbial Infections. *Biomacromolecules* **2022**, *23*, 592–608. [CrossRef]
7. Chakrapani, G.; Zare, M.; Ramakrishna, S. Current Trends and Definitions in High-Performance Antimicrobial Strategies. *Curr. Opin. Biomed. Eng.* **2022**, *23*, 100407. [CrossRef]

8. Yan, L.; Gopal, A.; Kashif, S.; Hazelton, P.; Lan, M.; Zhang, W.; Chen, X. Metal Organic Frameworks for Antibacterial Applications. *Chem. Eng. J.* **2022**, *435*, 134975. [\[CrossRef\]](#)
9. Chernousova, S.; Epple, M. Silver as Antibacterial Agent: Ion, Nanoparticle, and Metal. *Angew. Chem. Int. Ed.* **2013**, *52*, 1636–1653. [\[CrossRef\]](#) [\[PubMed\]](#)
10. Butkus, M.A.; Edling, L.; Labare, M.P. The Efficacy of Silver as a Bactericidal Agent: Advantages, Limitations and Considerations for Future Use. *J. Water Supply Res. Technol. -Aqua* **2003**, *52*, 407–416. [\[CrossRef\]](#)
11. Malmir, S.; Karbalaee, A.; Pourmadadi, M.; Hamed, J.; Yazdian, F.; Navaee, M. Antibacterial Properties of a Bacterial Cellulose CQD-TiO₂ Nanocomposite. *Carbohydr. Polym.* **2020**, *234*, 115835. [\[CrossRef\]](#)
12. Ma, S.; Zhan, S.; Jia, Y.; Zhou, Q. Superior Antibacterial Activity of Fe₃O₄-TiO₂ Nanosheets under Solar Light. *ACS Appl. Mater. Interfaces* **2015**, *7*, 21875–21883. [\[CrossRef\]](#)
13. Jia, Y.; Zhao, L. The Antibacterial Activity of Fluoroquinolone Derivatives: An Update (2018–2021). *Eur. J. Med. Chem.* **2021**, *224*, 113741. [\[CrossRef\]](#)
14. Au-Duong, A.-N.; Lee, C.-K. Iodine-Loaded Metal Organic Framework as Growth-Triggered Antimicrobial Agent. *Mater. Sci. Eng. C* **2017**, *76*, 477–482. [\[CrossRef\]](#) [\[PubMed\]](#)
15. Dong, X.; Liang, W.; Meziani, M.J.; Sun, Y.-P.; Yang, L. Carbon Dots as Potent Antimicrobial Agents. *Theranostics* **2020**, *10*, 671–686. [\[CrossRef\]](#) [\[PubMed\]](#)
16. Cui, F.; Ye, Y.; Ping, J.; Sun, X. Carbon Dots: Current Advances in Pathogenic Bacteria Monitoring and Prospect Applications. *Biosens. Bioelectron.* **2020**, *156*, 112085. [\[CrossRef\]](#)
17. Wang, B.; Song, H.; Qu, X.; Chang, J.; Yang, B.; Lu, S. Carbon Dots as a New Class of Nanomedicines: Opportunities and Challenges. *Coord. Chem. Rev.* **2021**, *442*, 214010. [\[CrossRef\]](#)
18. Kalaj, M.; Bentz, K.C.; Ayala, S., Jr.; Palomba, J.M.; Barcus, K.S.; Katayama, Y.; Cohen, S.M. MOF-Polymer Hybrid Materials: From Simple Composites to Tailored Architectures. *Chem. Rev.* **2020**, *120*, 8267–8302. [\[CrossRef\]](#)
19. Wang, B.; Chen, H.; Peng, S.; Li, X.-D.; Liu, X.; Ren, H.; Yan, Y.; Zhang, Q. Multifunctional Magnesium-Organic Framework Doped Biodegradable Bone Cement for Antibacterial Growth, Inflammatory Regulation and Osteogenic Differentiation. *J. Mater. Chem. B* **2023**. [\[CrossRef\]](#)
20. Stock, N.; Biswas, S. Synthesis of Metal-Organic Frameworks (MOFs): Routes to Various MOF Topologies, Morphologies, and Composites. *Chem. Rev.* **2012**, *112*, 933–969. [\[CrossRef\]](#)
21. Zhou, Z.; Li, B.; Liu, X.; Li, Z.; Zhu, S.; Liang, Y.; Cui, Z.; Wu, S. Recent Progress in Photocatalytic Antibacterial. *ACS Appl. Bio Mater.* **2021**, *4*, 3909–3936. [\[CrossRef\]](#) [\[PubMed\]](#)
22. Chen, R.; Yao, J.; Gu, Q.; Smeets, S.; Baerlocher, C.; Gu, H.; Zhu, D.; Morris, W.; Yaghi, O.M.; Wang, H. A Two-Dimensional Zeolitic Imidazolate Framework with a Cushion-Shaped Cavity for CO₂ Adsorption. *Chem. Commun.* **2013**, *49*, 9500. [\[CrossRef\]](#) [\[PubMed\]](#)
23. Taheri, M.; Ashok, D.; Sen, T.; Enge, T.G.; Verma, N.K.; Tricoli, A.; Lowe, A.; Nisbet, D.R.; Tsuzuki, T. Stability of ZIF-8 Nanopowders in Bacterial Culture Media and Its Implication for Antibacterial Properties. *Chem. Eng. J.* **2021**, *413*, 127511. [\[CrossRef\]](#)
24. Guo, Y.-F.; Fang, W.-J.; Fu, J.-R.; Wu, Y.; Zheng, J.; Gao, G.-Q.; Chen, C.; Yan, R.-W.; Huang, S.-G.; Wang, C.-C. Facile Synthesis of Ag@ZIF-8 Core-Shell Heterostructure Nanowires for Improved Antibacterial Activities. *Appl. Surf. Sci.* **2018**, *435*, 149–155. [\[CrossRef\]](#)
25. Liu, J.; Wu, D.; Zhu, N.; Wu, Y.; Li, G. Antibacterial Mechanisms and Applications of Metal-Organic Frameworks and Their Derived Nanomaterials. *Trends Food Sci. Technol.* **2021**, *109*, 413–434. [\[CrossRef\]](#)
26. Wijaya, C.J.; Ismadji, S.; Apamarta, H.W.; Gunawan, S. Facile and Green Synthesis of Starfruit-Like ZIF-L, and Its Optimization Study. *Molecules* **2021**, *26*, 4416. [\[CrossRef\]](#)
27. Yuan, Y.; Wu, H.; Lu, H.; Zheng, Y.; Ying, J.Y.; Zhang, Y. ZIF Nano-Dagger Coated Gauze for Antibiotic-Free Wound Dressing. *Chem. Commun.* **2019**, *55*, 699–702. [\[CrossRef\]](#)
28. Zhu, Y.; Mao, K.; Rong, J.; Zheng, Y.; Yang, D.; Zhang, T.; Qiu, F. Fabrication of Titanium Incorporation into Zeolitic Imidazolate Framework-L on Fabric Carrier for Visible-Light Driven Photocatalytic Antibacterial Activity. *Opt. Mater.* **2022**, *125*, 112085. [\[CrossRef\]](#)
29. Hao, L.; Jiang, R.; Gao, J.; Xu, J.; Tian, L.; Zhang, X.; Zhou, S.; Zhao, J.; Ren, L. Metal-Organic Framework (MOF)-Based Slippery Liquid-Infused Porous Surface (SLIPS) for Purely Physical Antibacterial Applications. *Appl. Mater. Today* **2022**, *27*, 101430. [\[CrossRef\]](#)
30. Wang, S.; Zang, B.; Chang, Y.; Chen, H. Synthesis and Carbon Dioxide Capture Properties of Flower-Shaped Zeolitic Imidazolate Framework-L. *CrystEngComm* **2019**, *21*, 6536–6544. [\[CrossRef\]](#)
31. Deacon, A.; Briquet, L.; Malankowska, M.; Massingberd-Mundy, F.; Rudić, S.; Hyde, T.; Cavaye, H.; Coronas, J.; Poulston, S.; Johnson, T. Understanding the ZIF-L to ZIF-8 Transformation from Fundamentals to Fully Costed Kilogram-Scale Production. *Commun. Chem.* **2022**, *5*, 18. [\[CrossRef\]](#) [\[PubMed\]](#)
32. Taheri, M.; Enge, T.G.; Tsuzuki, T. Water Stability of Cobalt Doped ZIF-8: A Quantitative Study Using Optical Analyses. *Mater. Today Chem.* **2020**, *16*, 100231. [\[CrossRef\]](#)
33. Kumar, R.; Kumari, S.; Rai, B.; Das, R.; Kumar, G. Effect of Nano-Cellulosic Fiber on Mechanical and Barrier Properties of Polylactic Acid (PLA) Green Nanocomposite Film. *Mater. Res. Express* **2019**, *6*, 125108. [\[CrossRef\]](#)

34. Hao, X.; Huang, L.; Zhao, C.; Chen, S.; Lin, W.; Lin, Y.; Zhang, L.; Sun, A.; Miao, C.; Lin, X.; et al. Antibacterial Activity of Positively Charged Carbon Quantum Dots without Detectable Resistance for Wound Healing with Mixed Bacteria Infection. *Mater. Sci. Eng. C* **2021**, *123*, 111971. [[CrossRef](#)] [[PubMed](#)]
35. Tripathi, K.M.; Ahn, H.T.; Chung, M.; Le, X.A.; Saini, D.; Bhati, A.; Sonkar, S.K.; Kim, M.I.; Kim, T. N, S, and P-Co-Doped Carbon Quantum Dots: Intrinsic Peroxidase Activity in a Wide PH Range and Its Antibacterial Applications. *ACS Biomater. Sci. Eng.* **2020**, *6*, 5527–5537. [[CrossRef](#)] [[PubMed](#)]
36. Nasir, A.M.; Md Nordin, N.A.H.; Goh, P.S.; Ismail, A.F. Application of Two-Dimensional Leaf-Shaped Zeolitic Imidazolate Framework (2D ZIF-L) as Arsenite Adsorbent: Kinetic, Isotherm and Mechanism. *J. Mol. Liq.* **2018**, *250*, 269–277. [[CrossRef](#)]
37. Wei, X.; Wang, Y.; Huang, Y.; Fan, C. Composite ZIF-8 with CQDs for Boosting Visible-Light-Driven Photocatalytic Removal of NO. *J. Alloys Compd.* **2019**, *802*, 467–476. [[CrossRef](#)]
38. Zhang, H.; Ming, H.; Lian, S.; Huang, H.; Li, H.; Zhang, L.; Liu, Y.; Kang, Z.; Lee, S.-T. Fe₂O₃/Carbon Quantum Dots Complex Photocatalysts and Their Enhanced Photocatalytic Activity under Visible Light. *Dalton Trans.* **2011**, *40*, 10822–10825. [[CrossRef](#)]
39. Makhetha, T.A.; Ray, S.C.; Moutloali, R.M. Zeolitic Imidazolate Framework-8-Encapsulated Nanoparticle of Ag/Cu Composites Supported on Graphene Oxide: Synthesis and Antibacterial Activity. *ACS Omega* **2020**, *5*, 9626–9640. [[CrossRef](#)]
40. Wang, Y.; Liu, X.; Wang, M.; Wang, X.; Ma, W.; Li, J. Facile Synthesis of CDs@ZIF-8 Nanocomposites as Excellent Peroxidase Mimics for Colorimetric Detection of H₂O₂ and Glutathione. *Sens. Actuators B Chem.* **2021**, *329*, 129115. [[CrossRef](#)]
41. Nasser Abdelhamid, H.; Mathew, A.P. Cellulose-Zeolitic Imidazolate Frameworks (CelloZIFs) for Multifunctional Environmental Remediation: Adsorption and Catalytic Degradation. *Chem. Eng. J.* **2021**, *426*, 131733. [[CrossRef](#)]
42. Rahaman, M.A.; Mousavi, B.; Naz, F.; Verpoort, F. Two-Dimensional Zeolitic Imidazolate Framework ZIF-L: A Promising Catalyst for Polymerization. *Catalysts* **2022**, *12*, 521. [[CrossRef](#)]
43. Baker, S.N.; Baker, G.A. Luminescent Carbon Nanodots: Emergent Nanolights. *Angew. Chem. Int. Ed.* **2010**, *49*, 6726–6744. [[CrossRef](#)] [[PubMed](#)]
44. Wei, X.; Cheng, F.; Yao, Y.; Yi, X.; Wei, B.; Li, H.; Wu, Y.; He, J. Facile Synthesis of a Carbon Dots and Silver Nanoparticles (CDs/AgNPs) Composite for Antibacterial Application. *RSC Adv.* **2021**, *11*, 18417–18422. [[CrossRef](#)] [[PubMed](#)]
45. Devi, P.; Saini, S.; Kim, K.-H. The Advanced Role of Carbon Quantum Dots in Nanomedical Applications. *Biosens. Bioelectron.* **2019**, *141*, 111158. [[CrossRef](#)]
46. Li, P.; Han, F.; Cao, W.; Zhang, G.; Li, J.; Zhou, J.; Gong, X.; Turnbull, G.; Shu, W.; Xia, L.; et al. Carbon Quantum Dots Derived from Lysine and Arginine Simultaneously Scavenge Bacteria and Promote Tissue Repair. *Appl. Mater. Today* **2020**, *19*, 100601. [[CrossRef](#)]
47. Zhang, H.; Liu, D.; Yao, Y.; Zhang, B.; Lin, Y.S. Stability of ZIF-8 Membranes and Crystalline Powders in Water at Room Temperature. *J. Membr. Sci.* **2015**, *485*, 103–111. [[CrossRef](#)]
48. Ahmad, N.; Md Nordin, N.A.H.; Jaafar, J.; Nik Malek, N.A.N.; Ismail, A.F.; Yahya, M.N.F.; Mohd Hanim, S.A.; Abdullah, M.S. Eco-Friendly Method for Synthesis of Zeolitic Imidazolate Framework 8 Decorated Graphene Oxide for Antibacterial Activity Enhancement. *Particuology* **2020**, *49*, 24–32. [[CrossRef](#)]
49. Yuan, Y.; Zhang, Y. Enhanced Biomimic Bactericidal Surfaces by Coating with Positively-Charged ZIF Nano-Dagger Arrays. *Nanomед. Nanotechnol. Biol. Med.* **2017**, *13*, 2199–2207. [[CrossRef](#)]
50. Riduan, S.N.; Zhang, Y. Nanostructured Surfaces with Multimodal Antimicrobial Action. *Acc. Chem. Res.* **2021**, *54*, 4508–4517. [[CrossRef](#)]
51. Zhang, X.; Li, H.; Miao, W.; Shen, Q.; Wang, J.; Peng, D.; Liu, J.; Zhang, Y. Vertically Zeolitic Imidazolate Framework-L Coated Mesh with Dagger-like Structure for Oil/Water Separation. *AIChE J.* **2019**, *65*, e16596. [[CrossRef](#)]

Disclaimer/Publisher's Note: The statements, opinions and data contained in all publications are solely those of the individual author(s) and contributor(s) and not of MDPI and/or the editor(s). MDPI and/or the editor(s) disclaim responsibility for any injury to people or property resulting from any ideas, methods, instructions or products referred to in the content.